Geophysical Journal International

Geophys. J. Int. (2016) **204,** 1801–1816 doi: 10.1093/gji/ggv556
GJI Seismology

Effects of realistic topography on the ground motion of the Colombian Andes – A case study at the Aburrá Valley, Antioquia

Doriam Restrepo,[1,*] Jacobo Bielak,[1] Ricardo Serrano,[2] Juan Gómez[3] and Juan Jaramillo[3]

[1] *Department of Civil and Environmental Engineering, Carnegie Mellon University, Pittsburgh, PA* 15213-3890, *USA. E-mail: drestre6@eafit.edu.co*
[2] *Applied Mechanics Group, Universidad EAFIT, Medellín, Colombia*
[3] *Departamento de Ingeniería Civil, Universidad EAFIT, Medellín, Colombia*

Accepted 2015 December 30. Received 2015 December 23; in original form 2015 May 10

SUMMARY

This paper presents a set of deterministic 3-D ground motion simulations for the greater metropolitan area of Medellín in the Aburrá Valley, an earthquake-prone region of the Colombian Andes that exhibits moderate-to-strong topographic irregularities. We created the velocity model of the Aburrá Valley region (version 1) using the geological structures as a basis for determining the shear wave velocity. The irregular surficial topography is considered by means of a fictitious domain strategy. The simulations cover a $50 \times 50 \times 25$ km^3 volume, and four $M_w = 5$ rupture scenarios along a segment of the Romeral fault, a significant source of seismic activity in Colombia. In order to examine the sensitivity of ground motion to the irregular topography and the 3-D effects of the valley, each earthquake scenario was simulated with three different models: (i) realistic 3-D velocity structure plus realistic topography, (ii) realistic 3-D velocity structure without topography, and (iii) homogeneous half-space with realistic topography. Our results show how surface topography affects the ground response. In particular, our findings highlight the importance of the combined interaction between source-effects, source-directivity, focusing, soft-soil conditions, and 3-D topography. We provide quantitative evidence of this interaction and show that topographic amplification factors can be as high as 500 per cent at some locations. In other areas within the valley, the topographic effects result in relative reductions, but these lie in the 0–150 per cent range.

Key words: Numerical solutions; Earthquake ground motions; Site effects; Wave propagation; South America.

INTRODUCTION

Topographic site effects have long been recognized as major contributors to seismic wave amplification. In general, a consistent pattern of severe structural damage has been reported on structures located at the top and/or on the slopes of topographic irregularities after the occurrence of large events (e.g. Paolucci 2002; Çelebi *et al.* 2010; Hough *et al.* 2011). Instrumental studies validate primary estimates from field observations (e.g. Kawase & Aki 1990; Hartzell *et al.* 1994; Spudich *et al.* 1996; Donati *et al.* 2001; Buech *et al.* 2010; Pischiutta *et al.* 2010; Lovati *et al.* 2011). In particular, field records exhibit a zone of amplification that takes place near mountain tops at wavelengths comparable to the mountain's width. Reductions occur near the bottom or at concave topographic features, while complex patterns of amplification/deamplification with significant spatial variability are also exhibited along the slopes (Geli *et al.* 1988; Assimaki *et al.* 2005; Maufroy *et al.* 2012).

In the South America scene, Çelebi (1987) reported evidence of topographic amplification after the 1985 March 3 Central Chile earthquake ($M_s = 7.8$). Spectral ratios derived from field experiments in Viña del Mar showed that amplifications from both topographic features and geologic variations took place at the ridges of Canal Beagle during the main event and the aftershocks. The frequency-dependent amplification correlates closely with the widespread damage experienced in buildings located along mountain ridges after the main event. Strong topographic effects can be expected in other regions of South America that exhibit similar topography and important seismicity because of the presence of large subduction faults. The Aburrá Valley (Antioquia, Colombia) is an example of such a region. This valley presents a complex tectonic regime, as it is located in a moderate intra-mountain depression at the confluence of four lithospheric tectonic plates in the northern part of the Andean Block: the Nazca, and the Caribbean plates of oceanic affinity, in conjunction with the South America plate

*Now at: Departamento de Ingeniería Civil, Universidad EAFIT, Medellín, Colombia.

and the Panama micro plate (GSM 2006). Over the last years, the Aburrá Valley region has been exposed to important distant events (>160 km), particularly the 1979 November 23 Central Colombia ($M_s = 6.7$), and the 1992 October 18 Atrato ($M_w = 7.1$) earthquakes. Geological evidence suggests important tectonic activity along its main structural systems. Seismic hazard analyses suggest potentially active ($M_w = 7$) seismic faults within the region (GSM 2006). Residual soil and hill-slope deposits occupy most of the Aburrá Valley slopes. The elongated valley has a total length of 60 km. It has a width of about 7 km near the centre of the valley, narrowing down northeast following the river's natural course. The north and east parts of the valley are surrounded by older erosion structures known as the Santa Elena (2750 m.a.s.l) and the San Pedro (2800 m.a.s.l) land surfaces (Aristizábal *et al.* 2005).

The Aburrá Valley metropolitan area consists of ten municipalities including the state capital Medellín. As of the first half of the 20th century, Medellín became the most important financial hub of Northwestern Colombia. The city became then an important centre of opportunity although by 1950 segregation shaped two types of urban areas (Echeverry & Orsini 2010). New arrivals started an irregular process of urbanization via self-housing at the northern end of the city and the eastern and western slopes of the mountains. By contrast, middle and upper classes urbanized the centre and southern ends of the valley following established construction norms for well-engineered buildings (Betancur 2007). To date, the contrast in the building inventory within the city still remains. Recent studies suggest that for Medellín alone, 51 per cent of its current structural systems corresponds to low-rise unreinforced masonry buildings (URM), prevailing at the slums, and prohibited by the current Colombian seismic provisions (NSR-10 2010). Conditions worsen higher up the slopes where construction quality dramatically reduces. A similar pattern of low-quality housing is exhibited at the remaining municipalities of the Aburrá Valley metropolitan area. Here, the percentage of unauthorized URM buildings reaches 67 per cent of the combined building constructed area (Osorio 2015). Presently, the valley houses about 3.8 million people, (∼8 per cent of Colombia's population). The valley large demographics in conjunction with the high rates of low-performance structural systems underline the need for an accurate assessment of the seismic hazard. Numerical simulation provides a useful tool for this purpose.

Past numerical simulations that consider realistic topography have been restricted to small computational domains representing either, large volumes of the Earth's crust subjected to low-frequency earthquake sources, for example, Komatitsch *et al.* (2004), (516 km × 507 km × 60 km, $f_{max} = 0.5$ Hz); Ma *et al.* (2007) (209.6 km × 120 km × 46 km, $f_{max} = 0.5$ Hz); Lee *et al.* (2008, 2009a) (101.9 km × 87.5 km × 102.89 km, $f_{max} = 1.0$ Hz), or small domains in conjunction with high-frequency source events, for example, Lee *et al.* (2009b), (∼ 4 km × 4 km × 10 km, $f_{max} \sim 10$ Hz). In this study, we take another step in the direction of realistic 3-D modelling and conduct a set of deterministic high-frequency ($f_{max} = 5$ Hz) 3-D ground motion simulations for the Aburrá Valley. The region of study comprises a 50 km × 50 km × 25 km volume in conjunction with four $M_w = 5$ rupture scenarios along one segment of the Romeral fault, a significant source of seismic activity of Colombia located ∼15 km from the city of Medellín. In particular, high frequency analyses allow one to capture the combined effect of small wavelengths created by topographic scattering, with effects due to the source location and the near-surface low-velocity structure. We incorporated the surface topography by implementing a *Virtual Topography* scheme (Restrepo & Bielak 2014) into *Hercules* (Tu *et al.* 2006), the wave propagation octree-based finite element simulator developed by the Quake Group at Carnegie Mellon University. Each rupture scenario was simulated using three different models: (i) realistic 3-D velocity structure with realistic topography, that is, complete model (CMP); (ii) realistic 3-D velocity structure without topography, that is, squashed model (SQD); and (iii) homogeneous half-space with realistic topography, that is, homogeneous model (HMG). Under the limitations of the 3-D velocity model and the earthquake representation, this study aims at qualitatively examining the main differences in ground motion between the three models with special emphasis on comparing CMP with SQD findings. Our results illustrate how a realistic topography modifies the ground response. Moreover, our findings highlight the importance of the combined interaction between source-effects, focusing, soft-soil conditions, and 3-D topography.

REGIONAL TECTONICS AND SEISMICITY

The tectonic environment of Colombia is controlled by the relative movement of the South American, the Nazca and the Caribbean plates. The Nazca oceanic plate is converging eastwards relative to the northwestern South America at 6–7 cm yr^{-1}, while the Caribbean plate moves 1–2 cm yr^{-1} to the east–southeast relative to the South American plate (Freymueller *et al.* 1993; Kellogg & Vega 1995). The Andean belt is a consequence of this intracontinental deformation through a continuous process of subduction, obduction, and accretion of oceanic terrains in the western and northwestern margins of Colombia since Paleozoic times (e.g. Bourgois *et al.* 1982; McCourt *et al.* 1984; Bourgois *et al.* 1987).

From west to east, the Colombian Andes consist of three subparallel mountain chains: the Occidental, Central and Oriental Cordilleras. These ranges trend NS and NE-SW following the contact boundaries of the plates. Shallow seismicity in Colombia is mostly constrained to the Andes range, which exhibits a strong correlation with the borders of the Cordilleras (Pulido 2003). According to París *et al.* (2000), approximately 47 Quaternary faults are associated with the Colombian Cordilleras. Of these, two major faults are traditionally associated with the largest share of the country's seismic activity. The first is the Romeral Fault System (RFS), which extends along the Cauca Valley and the Central Cordillera (see Fig. 1). With a total length of almost 700 km, it consists of three or four regional fractures with a diverse movement regime due to its long extension (Pulido 2003). South of 5°N the RFS has a right-lateral movement related to the oblique subduction of the Nazca plate. North of 5°N the direction of movement changes to left-lateral, apparently associated with the S-SE convergence of the Choco-Panamá Block (Taboada *et al.* 2000). The second fault is the Eastern Frontal fault system, which is the major geologic limit between the lowlands at the east, and the Andes range in the west. It consists of at least 10 sections with a combined length of 921.4 km that goes from Ecuador to the Venezuelan Andes in a typical foreland fold and thrust belt setting (París *et al.* 2000). Seismic activity is mostly restricted to the border of the Oriental Cordillera (Fig. 1).

The Aburrá Valley region (AVR) is a moderate intra-mountain depression located at the north end of the central range of the Colombian Andean region (Fig. 1). The surrounding mountains and plateaus can reach heights of between 2200 to 3000 m.a.s.l., with its lowest level located at 1300 m.a.s.l. The valley's geological setting consists of (i) a Paleozoic metamorphic basement, (ii) ultrabasic igneous rocks, (iii) a volcano-sedimentary sequence, (iv) intrusive

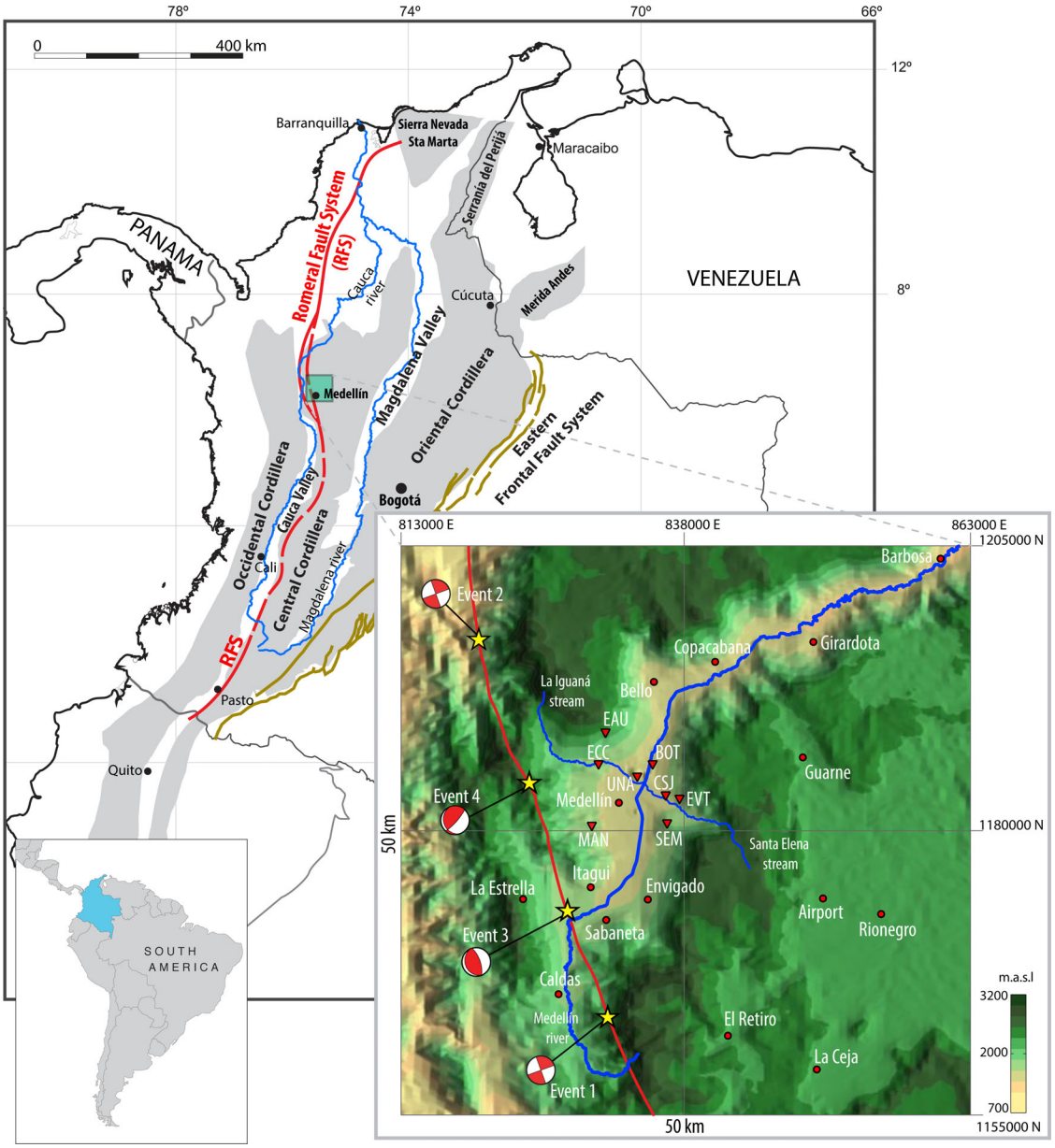

Figure 1. General location of the region of study. Grey areas depict the major topographic units of the Colombian Andes. The light green square represents the 50 × 50 km^2, 25 km deep, targeted domain for the 3-D ground motion simulations of the Aburrá Valley region. In red is the Romeral Fault System (RFS). Red dots represent the most important municipalities within the region. Stars represent the epicentres of the four 10 km deep rupture scenarios. Beach balls depict the focal mechanisms (see Table 1). Red triangles represent the locations of eight out of twenty eight strong ground motion stations within the city of Medellín. Modified map after Barrero *et al.* (2007).

granitoid bodies and (v) hillslope and alluvial sediments (Maya & Gonzales 1995). According to Aristizábal *et al.* (2005), the valley can be divided into three broad geomorphologic sectors, (i) a central portion comprised of broad alluvial plains bounded by moderate to gentle slopes, (ii) northern and southern parts consisting of narrow asymmetric valleys bounded by steep slopes and (iii) older erosion features that flank the valley to the north and the east, but are absent in the southwestern sector. The Medellín river and its two main tributaries, the Santa Helena and Iguaná streams, have deposited most of the alluvial deposits in the central and lowest portions of the valley, which vary between 3 and 200 m in depth (Adams & Jaramillo 2002). The steep slopes (>30 per cent) and most elevated parts of the valley are covered by a thick weathering profile. Depths of these weathered profiles and local conditions vary with location. They are thicker usually at gentle slopes (∼10 per cent) and become shallower on steep slopes as a consequence of erosion (Aristizábal *et al.* 2005).

Historic accounts from 1730 report 39 seismic events felt in the city of Medellín with intensities larger than III on the Modified Mercalli scale, five of them located under the city of Medellín with Mercalli values from III to V (Ramírez 1975). Recent seismic activity of relevant intensity for the city of Medellín has been limited to destructive far-field earthquakes (>160 km). The 1979 November 23 Central Colombia earthquake ($M_s = 6.7$), and the 1992 October 18 Atrato earthquake ($M_w = 7.1$), registered rock PGA of 0.03g, and 0.015g respectively (Adams & Jaramillo 2002). The 1992 event generated an estimated $US11 million loss to the city of Medellín. On the other hand, economic costs under the possible recurrence of

earthquake scenarios like the 1979 event were estimated 15 yr ago to be in the range of $US250 to $US300 million (Farbiarz *et al.* 2000; Adams & Jaramillo 2002). The 1999 January 25 Eje Cafetero Armenia earthquake ($M_w = 6.2$), which ruptured along a segment of the Romeral Fault System in the Eje Cafetero area was also felt in the Aburrá Valley region. PGAs of 0.014g/0.012g were registered at some stations of the local strong-motion network on the eastern/western slopes of the valley, although no economic losses were reported. Colombian seismic regulations estimate a moderate seismic hazard for the Aburrá Valley region (NSR-10 2010). Geological evidence, however, suggests an important tectonic activity along its main structural systems. In average, each one of the ten municipalities of the metropolitan area of the Aburrá Valley is less than 25 km from a potentially active $M_w = 7$ seismic fault. Of particular note, the Romeral fault system is just 5 km from the municipality of Caldas, and only 15 km from the city of Medellín. A rupture along a nearby segment of the Romeral fault is regarded as the worst-case scenario for the region where PGA up to 0.4g are expected (GSM 1999). Evidence from recent seismological surveys indicates that PGAs for a return period of 475 years are dominated by near sources ($\leq$20 km) of moment magnitudes $M_w \geq 6.5$ (GSM 2006).

RUPTURE SCENARIOS AND VELOCITY MODEL

To investigate the relative ground motions in different areas of the region of study and to further illustrate the combined effect of topography with near-source rupture scenarios, we propose to analyse the 50 km × 50 km, 25 km deep region shown in Fig. 1. The region covers the entire city of Medellín (population ~2.5 million), and several other municipalities of regional importance. North of the city of Medellín are the municipalities of Barbosa, Girardota, Copacabana and Bello (combined population of ~630 000 inhabitants). South of the city of Medellín are the municipalities of Itagui, Envigado, Sabaneta, La Estrella and Caldas (combined population of ~680 000 inhabitants). The nine municipalities combined are locally known as the Aburrá Valley metropolitan area. The domain of study also considers the highland municipalities of Guarne, Rionegro, El Retiro and La Ceja located at the elevated region of the San Nicolas Valley east of the city of Medellín (~2100 m.a.s.l—combined population of ~240 000 inhabitants). The selected domain comprises every major topographic irregularity within the region including several rupture scenarios from the Romeral Fault.

The segment of the Romeral fault enclosed in the proposed domain encompasses potential rupture zones with long return periods. Strong motion events have not been recorded on this segment thus far, nor have realistic kinematic models been developed for the region either. In the present simulations, the effects of an extended rupture front are sidestepped by assuming earthquake events of low magnitude ($M_w = 5.0$), which can accurately be modelled as double-couple kinematic point sources.

We simulated 3-D wavefields generated by four source scenarios 10 km deep in order to study propagation path effects due to sources arriving from different directions. Other parameters representatives of left-lateral strike-, thrust- and oblique-faults respectively are shown in Table 1. Since our primary goals are to examine the relative differences in ground motion due to topographic effects, rather than on actual values of ground motion per se, and to control the range of frequencies of excitation, in this study we assume a Ricker pulse source slip function of maximum frequency $f_{max} = 5$ Hz, and constant strike of 160° consistent with the average orientation of the Romeral fault in our domain. In order to limit the effect of the specific variability of the source with frequency, we include results of the ratios of response spectra with and without topography, at various locations, in addition to other results. Time responses for other types of source slip-functions can be readily obtained by Fourier synthesis of the frequency domain components of our results, times the frequency domain ratio between slip functions using Fast Fourier Transforms.

Our development of the velocity model (version 1) for the AVR starts with the work of Acevedo (2011) as a point of departure. The reference work recognizes 17 geological structures for which it establishes their internal geometry, presumable contact, and eventual deep geologic formations based upon information from local geological studies and geophysical data throughout the region. The reference study renders the most likely geological setting, including the terrain elevation through north-south vertical sections every 2 km over a nearly rectangular area of 49.541 km × 40.5 km, and 30 km deep. We incorporated the geological information into a computer algorithm that uses Delaunay triangulation to create interpolation rules aimed at identifying the corresponding geological unit enclosed by two adjacent sections (Serrano 2014). Because the computational domain is larger than the geological covered area, the velocity model includes an artificial geologic unit of generic homogeneous material intended to fill volumes where information is lacking. This simplification mostly affects the south end of the domain at the Caldas, el Retiro and La Ceja municipalities. Results from the first rupture scenario will be the ones more affected by this assumption. In particular, the artificial material interface will likely enhance unrealistic edge effects in the southern part of the domain. Thus, ground motion stemming from this scenario is the least realistic. On the other hand, the other three events occur well north of the homogeneous block. Part of the wave energy will be reflected from the interface but this is small compared with the energy of the direct waves, which occur entirely within the part of the model that is better constrained. Consequently, we deem the results of the remaining events to be reasonable and consistent with the velocity model north of the interface.

Table 1. Double-couple point-source parameters. Latitude and longitude are expressed in the Colombian local coordinate system: 1 000 000N(4°35′56.57″N); 1 000 000E(74°4′51.30″W).

Event	Strike (°)	Dip (°)	Rake (°)	Long (E)	Lat (N)	Depth (km)	Foc Mech.
1	160	90	0	831 024	1 163 562	10	
2	160	90	0	819 828	1 196 764	10	
3	160	20	90	827 633	1 172 945	10	
4	160	20	30	824 299	1 184 232	10	

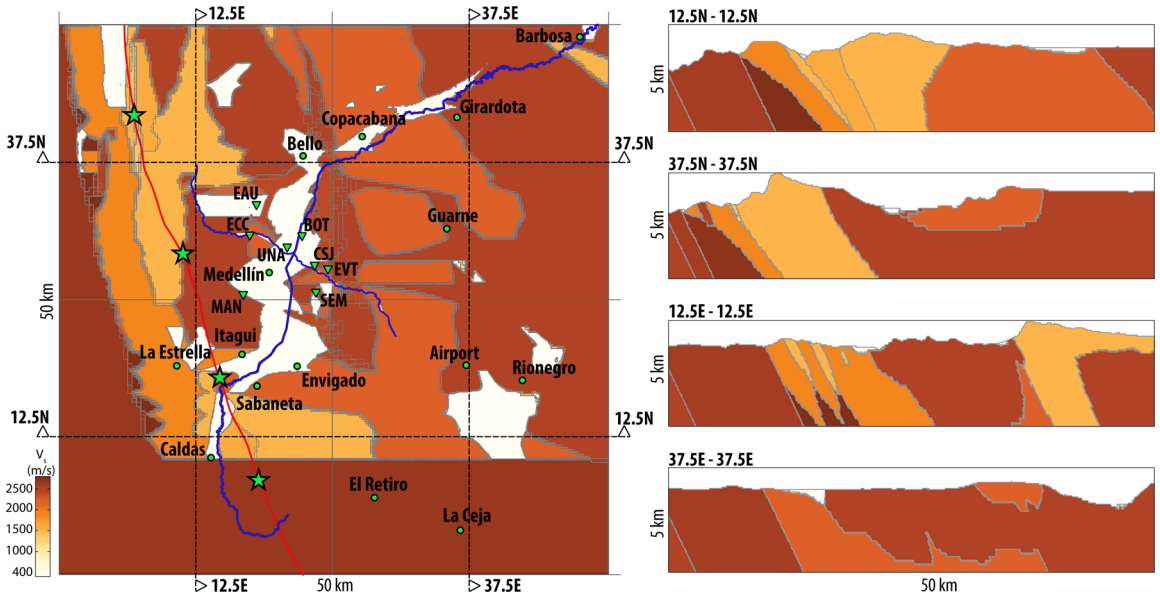

Figure 2. Plane and vertical cuts of shear wave velocity of the region of study. The proposed *S*-wave structure reasonably detects the soft deposits of alluvial sediments ($V_s = 400$ m s^{-1}) along the Medellín River bed, as well as the soft soil deposits east of the city of Medellín at the Rionegro municipality.

Fig. 2 depicts the free surface shear wave velocities according to the proposed 3-D wave structure. The velocity model reasonably identifies the Quaternary deposits along the Medellín River bed. Soft soil deposits at the San Nicolas Valley (SNV) are also detected. The slowest shear-wave velocity in the regional model corresponds to these Quaternary deposits ($V_s = 400$ m s^{-1}). *P*-wave velocities are computed by assuming a constant Poisson's ratio of $\nu = 0.3$ in every geologic structure. Throughout the entire domain, the density ρ is constrained to lie between $2000\,\mathrm{kg\,m^{-3}} \leq \rho \leq 3000\,\mathrm{kg\,m^{-3}}$. Due to limited information, and with the interest of obtaining a baseline calculation, intrinsic attenuation is not considered in the present material model. Our simulations will thus generate larger amplitudes that might be otherwise expected. On the other hand, ratios among findings are less likely to be affected by this hypothesis. In the same direction, this first version of the model assumes the seventeen geologic units of the reference study to be homogeneous. This can be interpreted as an average of any material heterogeneity around each subregion. The mechanical properties of each homogeneous body were based upon proposed estimates according to the type of the geological unit. The assumption of piecewise homogeneous bodies preserves the high complexity, heterogeneity of the geologic units within the region, and prominent internal geometric variations of the geological setting. This allows us to capture possible focusing effects due to deeper geologic formations as reported by other authors (e.g. Gao *et al.* 1996; Hartzell *et al.* 1997). Other large-scale earthquake simulations have also found it acceptable to resort to the assumption of piecewise homogeneous geologic units on their simulations (e.g. Paolucci 2002; Gvirtzman & Louie 2010; Maufroy *et al.* 2012; Shani-Kadmiel *et al.* 2012).

COMPUTATIONAL METHOD

Our Virtual Topography (VT) approach for representing the free-surface topography within an octree representation (Restrepo & Bielak 2014) adopts fictitious domain ideas (Saulev 1963) and embeds a domain Ω of free boundary $\partial\Omega = \partial\Omega_N \cup \partial\Omega_D$ into an augmented body $\tilde{\Omega}$ of homogeneous traction-free boundary $\partial\tilde{\Omega}$. The augmented domain is discretized using an unstructured octree-based mesh composed of trilinear cubic finite elements (see 2-D version in Fig. 3).

Applying standard Galerkin ideas to the Navier's equations one derives the well-known semi-discrete version of the equation of elastodynamics

$$\mathbf{M}\ddot{\mathbf{u}} + \mathbf{K}\mathbf{u} = \mathbf{P} \tag{1}$$

in which, **M**, and **K** are the sparse mass and stiffness matrices, **P**, and **u** are the vectors of nodal forces and nodal displacements respectively. In our formulation, material attenuation is considered by adding to the left side of eq. (1) the term $\mathbf{C}\dot{\mathbf{u}}$. The damping matrix **C** is assumed as a linear combination of the mass and stiffness matrices, that is, viscous Rayleigh type model. In a second damping model, denoted as *BKT*, the material is considered as a combination of generalized Maxwell elements. This form of damping allows one to simulate a constant quality factor Q within the range of frequencies of interest (Bielak *et al.* 2011). Due to its simplicity viscous damping is favoured as the material attenuation model in VT, although for the particular case of this study intrinsic damping is set to zero due to constraints of the first version of the *S*-wave velocity model of the AVR.

The elements of the matrices **M** and **K** in eq. (1) are 3×3 block matrices of the form:

$$\mathbf{M}_{ij} = \int_{\tilde{\Omega}} \alpha\rho\phi_i\phi_j\mathbf{I}\,\mathrm{d}\tilde{\Omega}\,, \tag{2}$$

$$\mathbf{K}_{ij} = \int_{\tilde{\Omega}} \alpha(\mu+\lambda)\nabla\phi_i\nabla\phi_j^{\mathrm{T}}\,\mathrm{d}\tilde{\Omega} + \int_{\tilde{\Omega}} \alpha\mu\nabla\phi_i^{\mathrm{T}}\nabla\phi_j\mathbf{I}\,\mathrm{d}\tilde{\Omega}\,, \tag{3}$$

in which, ϕ_i is the standard global basis function associated with the i-th node, λ, μ, and ρ denote the Lamé constants, and density of the material, while α represents the penalizing material factor in the augmented region $\tilde{\Omega} \setminus \Omega$. Eqs (2) and (3) exhibit the same functional form as in the traditional discrete version of the elastodynamic equations (e.g. Bao *et al.* 1998). The only difference from the fictitious domain approach arises when computing the mass and stiffness contributions of nodes whose global function partially covers void areas. Here, the evaluation of the integrals is limited

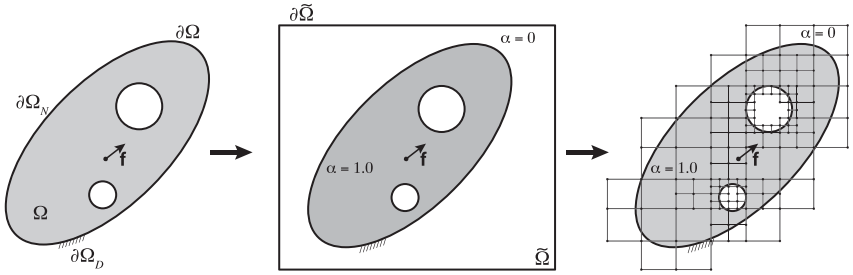

Figure 3. Fictitious domain scheme (2-D representation). The domain Ω is embedded into an augmented domain $\tilde{\Omega}$ of traction-free surface $\partial\tilde{\Omega}$. The enlarged domain is further discretized with an unstructured octree-mesh. Elements completely outside Ω are eliminated for numerical stability.

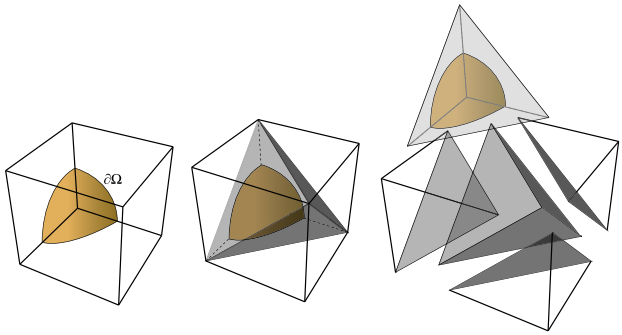

Figure 4. Virtual topography decomposition after Restrepo & Bielak (2014). A cubic topography-intercepted element is partitioned into five non-overlapping constant tetrahedral elements.

to the zones that contain matter due to variations of α along the traction-free boundary $\partial\Omega$.

VT manages the variations of α by partitioning every intersected cubic element into five tetrahedra of constant strain and homogeneous material (see Fig. 4). As a result, gradients and material properties become constants that are taken out of the integrals in eq. (3). This reduces the evaluation of discontinuous integrands to computing the volume enclosed by the tetrahedral elements. After simple algebraic manipulation, the stiffness matrix of the n-th tetrahedron is written as the product of its percentage of matter content β_n times the corresponding matrix of the complete n-th tetrahedron $\mathbf{k^t}_n$. The stiffness matrix of the parent cubic element $\mathbf{k^e}$ is obtained from the contribution of its children tetrahedral elements following standard assembling techniques:

$$\mathbf{k^e} = \sum_{n=1}^{5} \beta_n \mathbf{k^t}_n. \tag{4}$$

Stiffness scalability for the exterior topographic elements is the most salient feature of the method. Since every element of the octree mesh is a cube, the five stiffness matrices of the individual tetrahedral elements are computed at the beginning of the simulation. At simulation time, these are simply scaled by the size, material properties, and matter content β_n of the element in order to evaluate the nodal force contribution.

In the VT scheme the mass matrix of the topography-intercepted cubic element $\mathbf{m^e}$ is also assumed to share scalability properties as in eq. (4).

$$\mathbf{m^e} = \sum_{n=1}^{5} \beta_n \mathbf{m^t}_n. \tag{5}$$

As a result, the eigenvalues of a partially filled tetrahedron are the same as those of a tetrahedron totally filled with the same material. This is important from a computational point of view, as this renders a time step for explicit dynamics almost the same as that of the flat surface case (Rozycki *et al.* 2008; Restrepo & Bielak 2014). The enclosed topographic volumes within each tetrahedra are computed by adopting the 56 symmetric quadrature rule derived by Shunn & Ham (2012) using a cubic closed-packed lattice arrangement. This strategy symmetrically queries the tetrahedron volume, which eliminates the occurrence of clusters of quadrature points likely to occur when a cube to tetrahedron double transformation of conventional Gauss points is implemented.

GROUND MOTION SIMULATION PARAMETERS

Each rupture scenario is simulated under three assumptions regarding the macroscopic irregularities and the crustal velocity properties of the AVR. The first assumption employs the complete representation of the region by considering both the realistic velocity model of the crustal structure, and the realistic representation of its free-surface topography. We denote this model as the CMP since it contains all the major features that influence the ground motion throughout the region. Results from this simulation will be used as benchmark results for comparison with other models. The second numerical scenario disregards surface topography by artificially making the free surface flat. Flat-surface approximations are based on either 'squashed' or 'bulldozed' velocity models (e.g. Aagaard *et al.* 2008). The squashed surface approach levels the top surface at a certain elevation but retains the original thickness of the top layer (Quinay *et al.* 2012). Bulldozing the surface of the earth, on the other hand, strips away any material above some elevation and fills in any voids below this elevation with some generic material (Aagaard *et al.* 2008). In general, which strategy to use to flatten the topography is chosen on a case by case basis. Here, we favour the squashed approach because it preserves the material properties at the free-surface level, and imposes only minor distortions to the internal geologic units after flattening the topography. We denote this model as the SQD model. The third example isolates the effects of topography from those of material heterogeneity. Topographic isolation is achieved by simplifying the 3-D velocity structure as if it were a homogeneous domain. This model is labelled as the HMG simulation with average material properties: $V_s = 2000$ m s^{-1}, $V_p = 4000$ m s^{-1}, and $\rho = 2200$ kg m^{-3}. Twelve large-scale numerical simulations were then performed for the AVR, that is, four rupture scenarios $\times$ three velocity structure models. Table 2 presents the details of the simulations parameters, and the computational resources used.

Table 2. Summary of simulation parameters and input data. All simulations were run in Kraken, the Cray XT5 parallel supercomputer at the National Institute for Computational Science, US. Kraken was decommissioned on 2014 April 30.

Analytics	3-D velocity structure Complete (CMP)	Squashed (SQD)	Homogeneous (HMG)
f_{max}	5.0 Hz	5.0 Hz	5.0 Hz
Topography	Yes	No	Yes
$V_{s_{min}}$	400 m s^{-1}	400 m s^{-1}	2000 m s^{-1}
Points per wavelength (p)	13.1	13.1	16.3
p_{min} entire mesh	8	8	8
Min. elem. size	6.10 m	6.10 m	24.41 m
Num. of elements	4 617 025 557	4 181 610 745	3 058 335 221
Num. of nodes	4 707 518 437	4 198 489 003	3 066 223 684
Time step Δt	0.0005 s	0.0005 s	0.0025 s
Sim. time	30 s	30 s	30 s
Num. of cores	9960	9960	3960
Cores usage time	5 hr, 27 min	4 hr, 38 min	1 hr, 42 min

REGIONAL EFFECTS

Fig. 5 illustrates the time evolution of the vertical (Z) component of the velocity wavefields of the first event for the three material models considered. Results from the HMG simulation preserve the expected P-wave radiation pattern associated with a double-couple strike-slip source, with only minor modifications from the surrounding topography (Fig. 5g). By contrast, for the CMP and SQD models no recognizable radiation pattern is preserved. In both simulations the internal velocity gradient modifies the spatial distribution of the first arrivals, (Figs 5a and d). CMP and SQD results are generally similar, although the SQD wavefields exhibit a smoother distribution (Figs 5a and d). The first sign of ground motion modifications due to topographic effects is seen by the different spatial distribution of the saturated area at the top of the mountain between the municipalities of Caldas and La Estrella (see white arrow in Figs 5a and d).

Since S-waves exhibit smaller wavelengths than P-waves, their interaction with external irregularities becomes more important. An example of this interaction is clearly seen from the HMG results. As Fig. 5(h) shows, the AVR topography creates a complex pattern of reflected and scattered wavefields as the S and surface waves travel through the domain. Even stronger complexities are exhibited by the wave fronts of the CMP and SQD simulations, as Figs 5(b) and (e) show. In the case of the SQD model, these wave-front distortions are consequence of the low wave-speed velocity Quaternary deposits plus geometric effects from the geologic units. These effects are also present in the CMP simulations; however, as suggested by the larger number of saturated areas present in Fig. 5(b), the distortions in the wave fronts are larger in the CMP results. Homogeneous conditions create only minor changes on the circular shape of the primary P wave front (see Fig. 5h). It seems that the only notable topographic effect for the P wave front under HMG conditions is the trace of reflected and scattered waves left behind as the primary waves move forward.

As the simulation progresses, a large amount of energy gets trapped in the domain (Figs 5c, f and i). Fig. 5(i) shows a heavily distorted, yet, still distinctive circular S-wave front, moving outwards in the HMG model. By contrast, substantial variations in the 3-D structure are largely responsible for the trapped energy and wave reverberations exhibited by the SQD model in Fig. 5(f). The CMP model also exhibits effects from the 3-D velocity structure, and, in addition, topography effects are again visible. For instance, near the Rionegro and Guarne municipalities, clear amplifications are notable in Fig. 5(c) due to the steep canyon effect. These municipalities are located at elevated regions compared to that of the epicentre; therefore, the amplification pattern is consistent with the standard behaviour of ground motion at highlands.

Fig. 6 shows the snapshots of the normal-to-fault velocity component of the velocity vector for the third event simulation. The similarities between Figs 6(a) and (d) in conjunction with the uniform radiation pattern shown in Fig. 6(g) indicate the low impact of topography on the characteristics of ground motion at the early stages of the shaking. This trend was also encountered in the discussion of the vertical component of the first event. Similarities between the CMP and SQD results still persist at $t = 6.0$s. Here, source radiation patterns of high complexity emerge as a result of changes in the source location, the direction of the fault movement, and the early response of the Quaternary deposits near the southern municipalities of the AVR (see Figs 6b and e). Again, the effects of the coarse irregularities are exhibited more clearly by the HMG results. The P-wave continues moving forward with an evident circular shape (Fig. 6h). As for the vertical component of the velocity vector of the first rupture scenario, the effects of topography on the first arrivals is limited to the generation of small amplitude surface waves. By contrast, at $t = 12$s the complex geometry of the surficial topography greatly affects the characteristics of ground motion. The S-wave front is significantly distorted and amplified as it passes through the Aburrá Valley depression and moves towards the elevated municipalities of Guarne and Rionegro (Figs 6c and f). Of greater relevance are perhaps the differences of the incoming, high-energy wave fronts generated by the SQD and CMP models. According to the SQD model, there is only one large energy wavefront followed by a cluster of small intensity wavefields (Fig. 6f). On the other hand, while the CMP results predict the same initial wave front, this wave front exhibits a larger amplitude, besides being followed by high energy wave fronts of similar intensity. As can be readily inferred from Fig. 6, CMP results trigger a larger response of the Quaternary deposits of the SNV than those set off from traditional SQD simulations. Similar patterns of amplification at the SNV from wave interactions with the eastern flank of the AVR depression are shown in Fig. 6(i).

TOPOGRAPHIC AMPLIFICATION FACTOR

Observations regarding the impact of the AVR topography become more apparent if one examines the quantitative evidence in terms

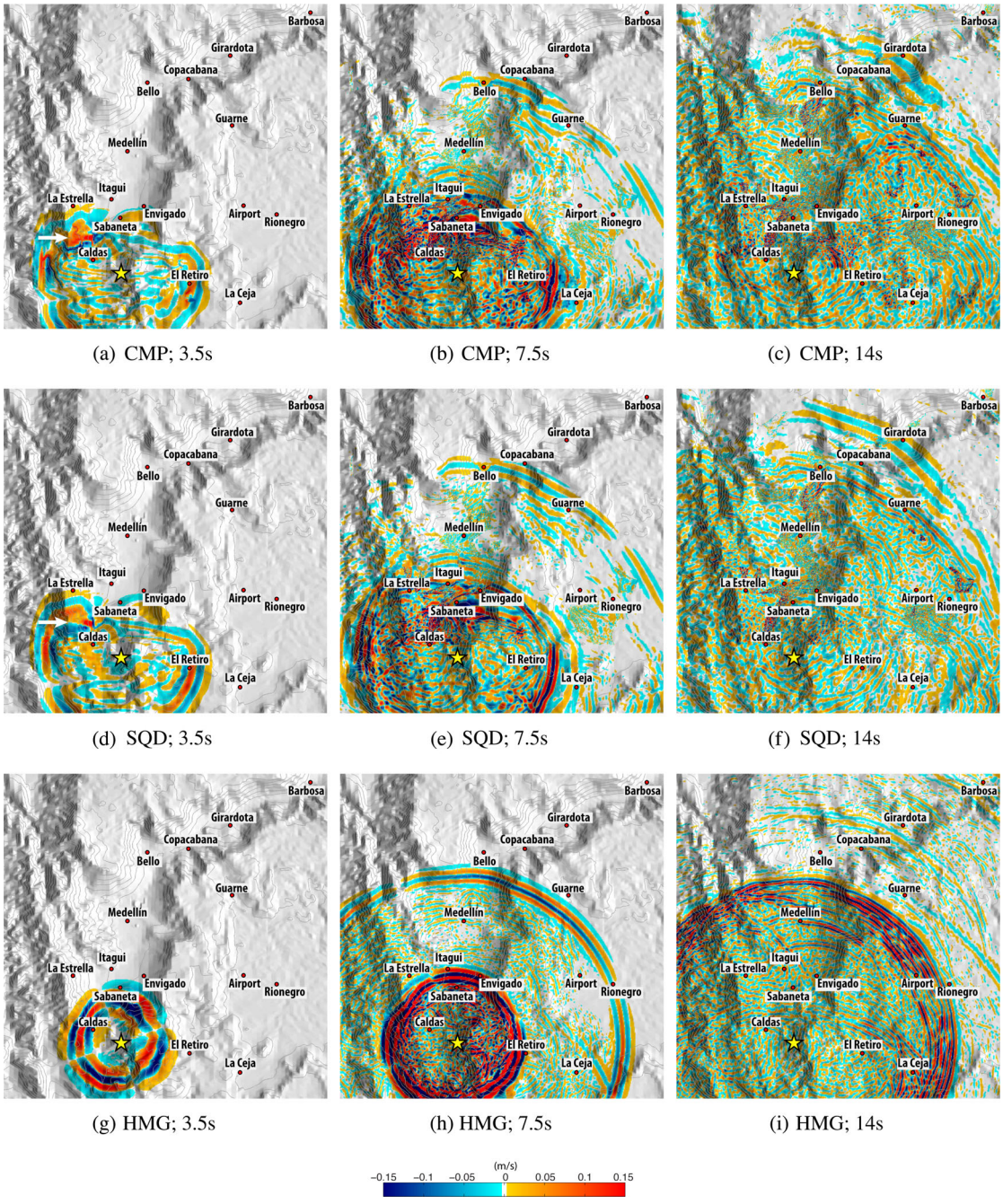

Figure 5. First scenario. Snapshots of the vertical component of the velocity wavefield for the CMP (a–c), SQD (d–f) and HMG (g–i) models. Columns represent time steps at 3.5, 7.5 and 14 s, respectively. The yellow-filled star illustrates the epicentre.

of topographic amplification factors (TAFs). The site-to-reference spectral ratio method (SRM; Borcherdt 1970) is the approach most commonly used to estimate topographic site effects (e.g. Tucker *et al.* 1984; Çelebi 1987; Pedersen *et al.* 1994). In general, the SRM assumes that the only difference between the measurements of ground motion at two different sites is the presence or absence of topographic features, all other factors remaining constant (Davis & West 1973; Field & Jacob 1995). In other words, the SRM implicitly assumes that at two different stations, the effects from the source, directivity, and the internal soil structure are similar. This is obviously not an acceptable assumption for the highly heterogeneous AVR and its near source earthquake scenarios. To overcome this problem other authors have used results from flat-free simulations as the reference site (e.g. Bouchon & Barker 1996; Lee *et al.* 2009a,b). From the numerical point of view this strategy is the natural step to follow since flat free-field simulations are the standard scheme in earthquake modelling. In this work we will follow the same approach and use the SQD results as the reference site. Specifically, we provide quantitative insight regarding the distribution of amplifications/reductions by topographic effects in terms of the topographic amplification factor (TAF) evaluated as:

$$\text{TAF} = \text{PGV Amplification} = \frac{\left(\text{PGV}_{\text{CMP}} - \text{PGV}_{\text{SQD}}\right)}{\text{PGV}_{\text{SQD}}} 100 \text{ per cent}, \quad (6)$$

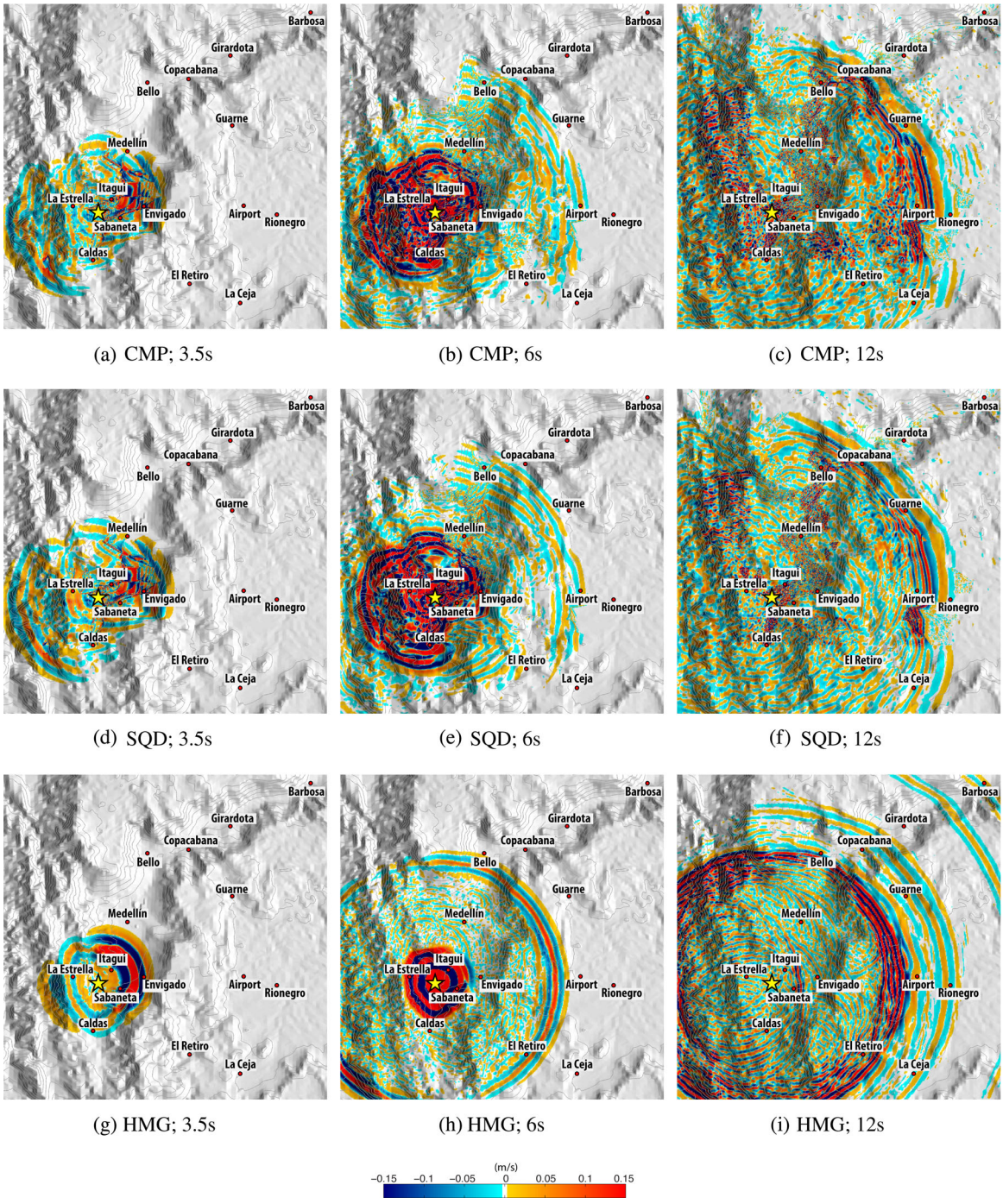

Figure 6. Third scenario. Snapshots of the normal to fault component of the velocity wave field for the CMP (a–c), SQD (d–f) and HMG (g–i) models. Columns represent time steps at 3.5, 6.0 and 12 s, respectively. The yellow-filled star denotes the epicentre.

in which PGV_{CMP} and PGV_{SQD} are peak ground velocities (PGV) from the CMP and SQD models respectively at a given location. The PGV at a particular site is computed as the largest magnitude of the ground velocity vector. We favour the representation in terms of ground velocity because it is closely related to the kinetic energy.

Fig. 7 presents the PGVs and TAFs distributions for the CMP and SQD simulations corresponding to the second and fourth rupture scenarios. The PGV distribution for the second rupture scenario exhibits most of its larger values near the epicentre (first row of Fig. 7), although within a relatively smaller area. This is basically the case of the CMP results where wavefield interactions with topography dissipate most of the seismic energy (Fig. 7a). As readily seen from Fig. 7(a), the slopes and the top of the mountain to the east of the epicentre present considerable reductions in their PGVs with respect to the model without topography Fig. 7(b). Examples of shielding effects such as those reported by Ma *et al.* (2007) are evident from Fig. 7(c). Note that for this rupture scenario the steep slopes north of the Bello municipality exhibit major reductions as consequence of this shielding effect. Zones of amplification due to the combined effect of local topography and source radiation are now observed at the river bed of the Santa Elena stream; one of the major tributaries of the Medellín river. Because the fourth earthquake scenario

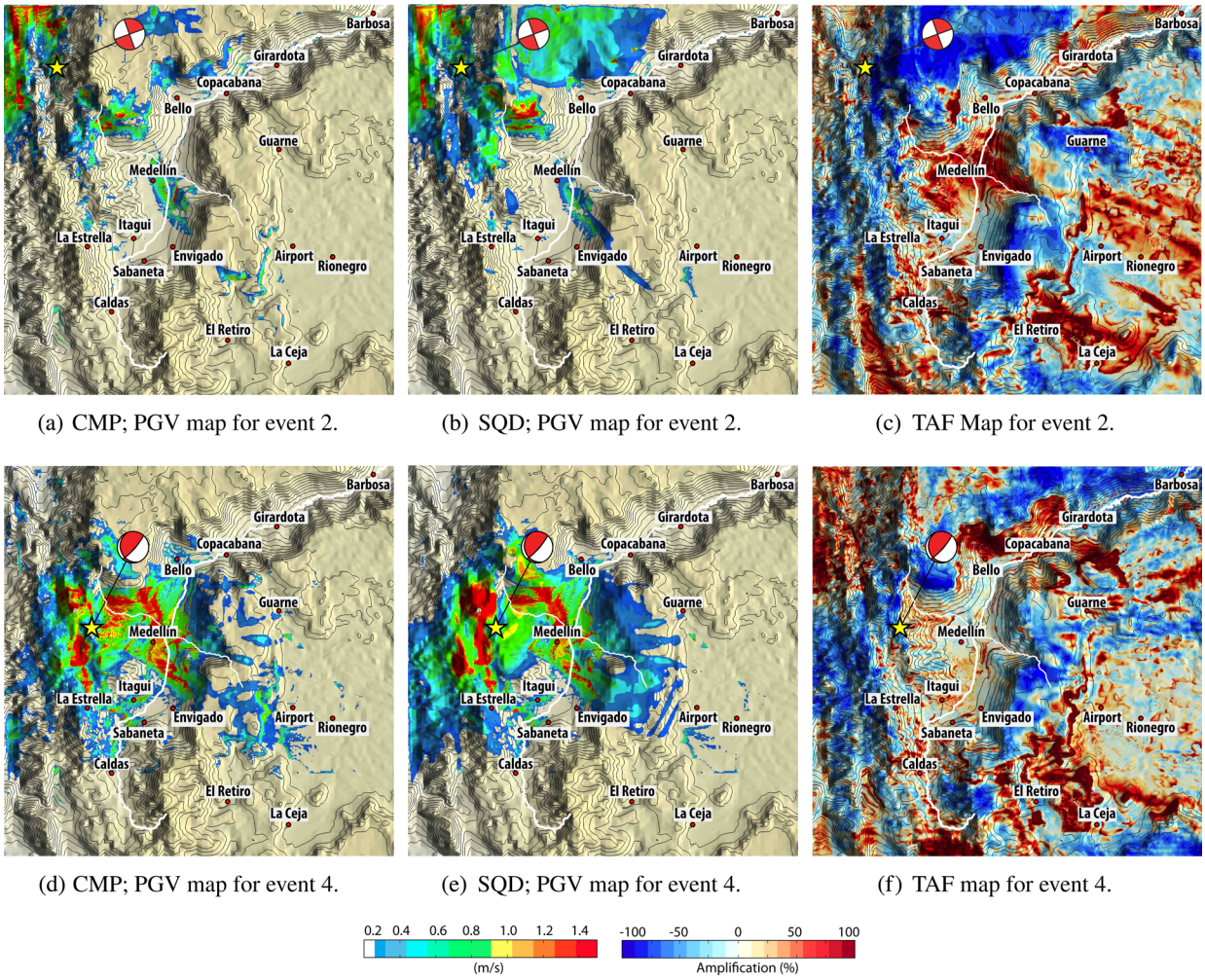

(a) CMP; PGV map for event 2. (b) SQD; PGV map for event 2. (c) TAF Map for event 2.

(d) CMP; PGV map for event 4. (e) SQD; PGV map for event 4. (f) TAF map for event 4.

Figure 7. PGV and TAF maps for events 2 and 4. The PGV at a particular site is computed as the largest magnitude of the ground velocity vector. The first row illustrates results for the second event. The bottom row depicts findings for the fourth rupture scenario. Warm/cool colours indicate amplification/reductions due to the AVR topography.

is closer to the centre of the domain, its PGV spatial distributions exhibits larger spreading and greater effects from basin interactions than the strike-slip scenarios (see bottom row of Fig. 7). Evidence of the latter can be found in the relatively low PGV amplification factors exhibited along the Quaternary deposits of the metropolitan area of the AVR (see Figs 7d and e). Evidence of major topographic effects, however, appears again as patterns of amplification throughout the SNV, and along the steep slopes of the mountain close to Bello, and Copacabana cities. The shielding effect along the top of the eastern flank of the Aburrá Valley depression is also visible (see Fig. 7f).

Fig. 8 consolidates the minimum (Fig. 8a), maximum (Fig. 8b) and envelope (Fig. 8c) of TAFs findings from the four earthquake scenarios. According to Fig. 8(c), at least three different areas that exhibit notable amplification are identified by the envelope response regardless of the particular event. The first is the zone close to the northwest corner of the domain (≈1200 m.a.s.l) where amplifications due to topographic effects reach values greater than 200 per cent. The second zone occurs throughout the Aburrá Valley metropolitan area (≈1500 m.a.s.l). This valley presents an average amplification between 100 and 150 per cent, although areas of rapid differential motion are identified over its slopes. Saturated areas of amplification are also visible. Detailed analyses presented in the following section show that some of these saturated zones can reach values up to 500 per cent. Interestingly, the foot and slope of the mountain flank in the vicinity of the Envigado municipality exhibit zones of amplification close to zero, that is, simulations with and without topography essentially coincide. On the other hand, amplifications larger than 200 per cent occur throughout the slopes of the mountain around the Bello municipality. The third amplification area consists of the elevated region east of the city of Medellín including the SNV (≈2000 m.a.s.l). Here, generalized amplifications of around 150 per cent are observed. Interestingly, the southern and western ends of the domain do not exhibit anomalous patterns of amplification due to the oversimplification of the extended homogeneous geologic unit. The almost horizontal reduction zone near the epicentre of the first event might however be related with the constraint imposed by the southerner homogeneous block of the crustal velocity structure. Other zones of deamplification are also clearly identifiable. As an example, the eastern and northern plateaus at the SNV valley and behind the Bello municipality are two particular zones where the TAFs envelope shows a trend towards reduction. Deamplifications prevail for the Bello plateau, while reductions for the SNV plateau are more notable in the adjacent area of the eastern elevated corner of the Aburrá Valley depression.

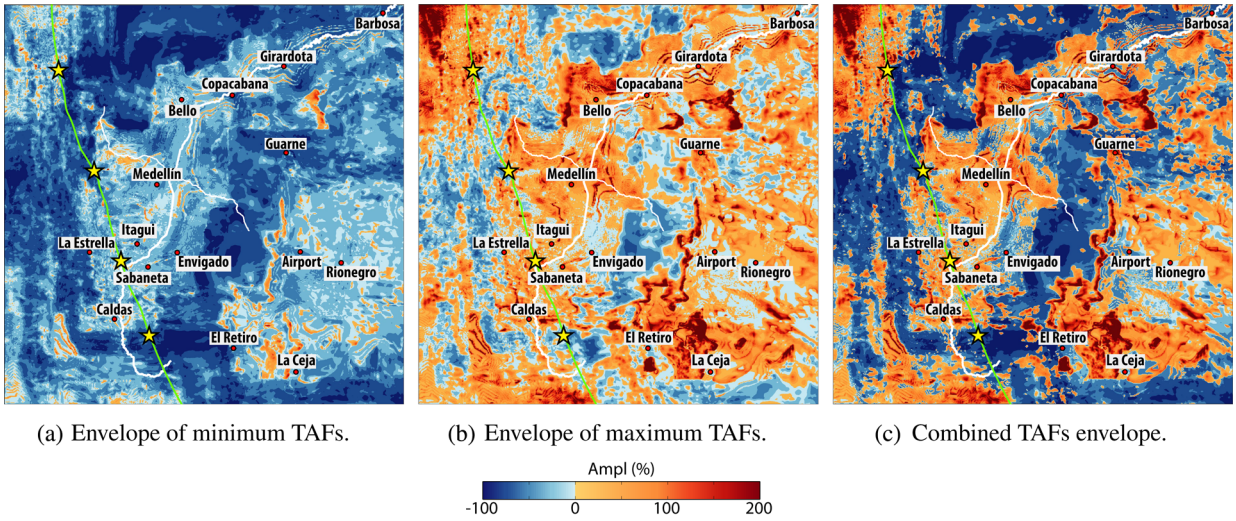

(a) Envelope of minimum TAFs. (b) Envelope of maximum TAFs. (c) Combined TAFs envelope.

Figure 8. Envelopes of topographic amplification factors from the four hypothetical events. Minimum TAFs (left), maximum TAFs (centre), and TAFs envelope (right). Yellow stars illustrate the epicentres of the four rupture models. The green line indicates the direction of the Romeral fault within the domain.

TAFs ALONG SELECTED CROSS-SECTIONS

To examine more closely the characteristics of the ground motion from the CMP and SQD simulations, we analyse TAFs of ground velocity on three east-west vertical cross-sections. Namely, sections 20N-20N, 30N-30N and 40N-40N, which are located 20, 30 and 40 km from the bottom of the domain. Fig. 9 presents the TAFs obtained along the free-surfaces of the selected cross-sections for the four events. Here, the TAFs are computed separately for each component of the synthetics of ground velocity, and for each rupture scenario. In general, the topographic irregularities generate positive TAF values (amplification) of up to 500 per cent at some specific locations. Reductions, although also present, always remain within the 0 to 100 per cent range, and more frequently closer to zero. The specific patterns of topographic amplification depend strongly on the particular component of ground motion, and greatly correlate with the soft-sedimentary deposits, source-radiation effects, and material interface effects.

Section 20N-20N, for instance, exhibits a concentration of local maxima in its eastern side. This could be related with source directivity effects (see Fig. 9b). The TAF for each velocity component is entirely due to differences in the topography. Maxima are observed at a number of locations independently of the seismic event. However, some components of ground motion are more sensitive to topographic amplification than others. An example of this is the site around 10 km in section 20N-20N. Here, the first earthquake event yields a vertical amplification of 350 per cent, while the EW and NS components exhibit only a minor topographic effect at the same location.

Section 30N-30N shows a concentration of local maxima over the western flank of the Aburrá Valley depression. Specifically, these local amplifications occur along the right slopes of the mountain (see Fig. 9c). Curiously, the top of the western flank does not exhibit a significant topographic amplification. These results challenge the traditional idea that topographic effects are always stronger at the top of the mountains. The first rupture scenario emerges as the major contributor of topographic amplification for the vertical component of the ground velocity vector, although the largest amplification, near 500 per cent, is generated by the fourth source model. On the other hand, the third and fourth source models contribute to the largest TAF in the EW velocity component. The NS velocity component does not show a particular preference for any of the four rupture scenarios.

Section 40N-40N presents substantial amplifications in the three components of ground velocity, all of them generated by the fourth rupture scenario. The NS velocity component shows a TAF of 430 per cent at the foothill of a local topographic feature located 30 km east of the origin. The EW and Z components on the other hand, exhibit their maxima halfway up the slope around 23 km east, with TAF of 460 and 270 per cent respectively (see Fig. 9d).

LOCAL RESPONSE

To examine the effects of topography at a local scale we now analyse synthetics of ground velocity at five stations of the strong ground motion network of the city of Medellín, namely SEM, CSJ, EAU, ECC and MAN (see red triangles in Fig. 1). Synthetic time series from the first rupture scenario for the fault parallel (V_{PL}) and the fault normal (V_N) components of the velocity vector are presented in Fig. 10. In every station the fault-parallel component exhibits the larger amplitudes as a consequence of the strike-slip nature of the first earthquake source. As expected, the first arrivals almost coincide in both simulations, although with slightly different traveltimes. Late phases on the other hand present notable differences. At station CSJ, for instance, strong late arrivals of large amplitude due to topographic effects are evident in both the fault normal and fault parallel components. Similar topographic effects in the form of strong late phases are displayed for station EAU, which is located halfway up to the NW plateau of the Aburrá Valley.

The Fourier spectra of the corresponding velocity components further illustrate the topographic effects. For instance, CMP results of station CSJ exhibit a dramatic increase in its peak Fourier amplitude close to $f \sim 2.5$ Hz in both horizontal components. With respect to SQD results the peak Fourier amplifications reach values as high as 9.5 and 6.4 for the fault normal and fault parallel components, respectively. Note that for the SQD results the peak amplitude occurs shifted to the right at around $f \sim 3.8$ Hz. This effect is more pronounced for the fault parallel component. Such marked differences could be related with interactions between edge effects and 3-D topography inasmuch as station CSJ is located at

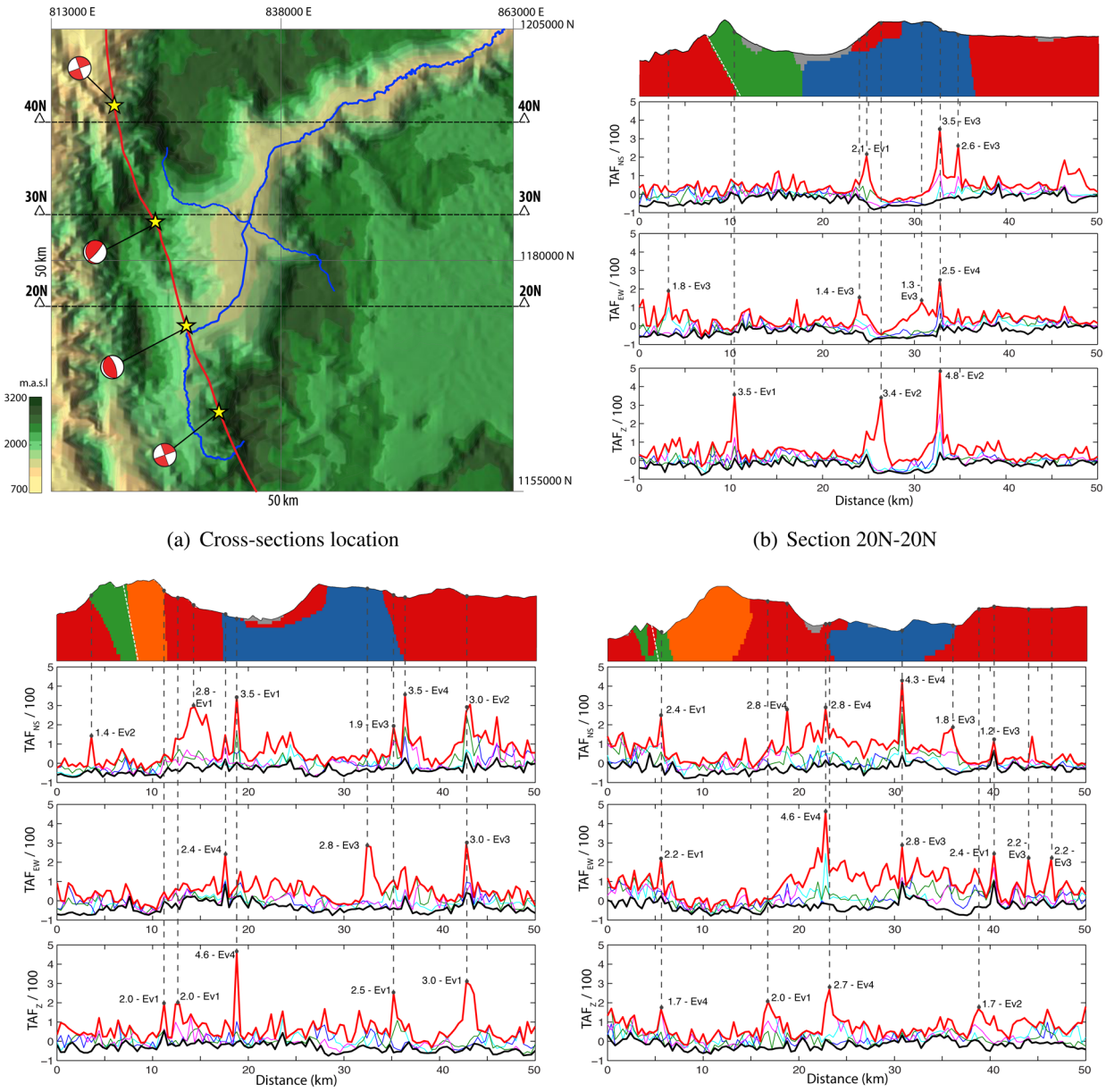

(a) Cross-sections location

(b) Section 20N-20N

(c) Section 30N-30N

(d) Section 40N-40N

Figure 9. TAF for different sections. The TAF are computed independently for the three components of the ground velocity vector (north–south, NS, east–west, EW, vertical, *Z*). The red and black thick lines represent the upper and lower bounds from all events. Cyan lines depict the TAF from the 1st source scenario. The blue, green and magenta lines depict the TAF results from the 2nd, 3rd and 4th rupture models. The colours of the cross-sections depict the geologic structures. The dotted white line illustrates the presumed location of the Romeral fault within the vertical section.

the foot of the eastern flank of the Aburra Valley depression, close to the right boundary of the Quaternary deposits (see Fig. 2). As expected, the CMP results dominate the peak Fourier amplitudes, though interestingly, the peak amplitude of the fault-normal component of station EAU is controlled by the SQD results. A similar situation is seen at station MAN, but for the fault-parallel component. A direct explanation of this behaviour is not yet clear. Further studies are needed to explore potential causes.

In Fig. 11, we now provide the local response in terms of the pseudo-acceleration response spectrum S_a(per cent g) (damping $\xi = 5$ per cent) at four selected stations corresponding to ground accelerations from the second and third events. Solid lines illustrate results from the second event, while dotted lines depict results from the third rupture model. CMP, SQD and response spectra ratios (RSR $= S_{a_{CMP}}/S_{a_{SQD}}$) are represented by the red, black and blue lines, respectively. As a general trend, results from the third event (dotted lines) dominate the peak amplitudes of S_a(per cent g). This condition, in addition to the similarities between response spectra, that is, RSR ~ 1.0 for stations BOT and MAN (see blue dotted lines) suggest that near source effects might be the dominant causes of ground motion for the third rupture scenario. On the other hand, the response at stations BOT and MAN for the second rupture scenario reach RSR ~ 2 in the short period range ($\leq$1s), which indicates a larger influence of topography conditions. On the contrary, stations UNA y EVT present larger variations in their RSR irrespective of the seismic source. Generally, results from the second event at stations

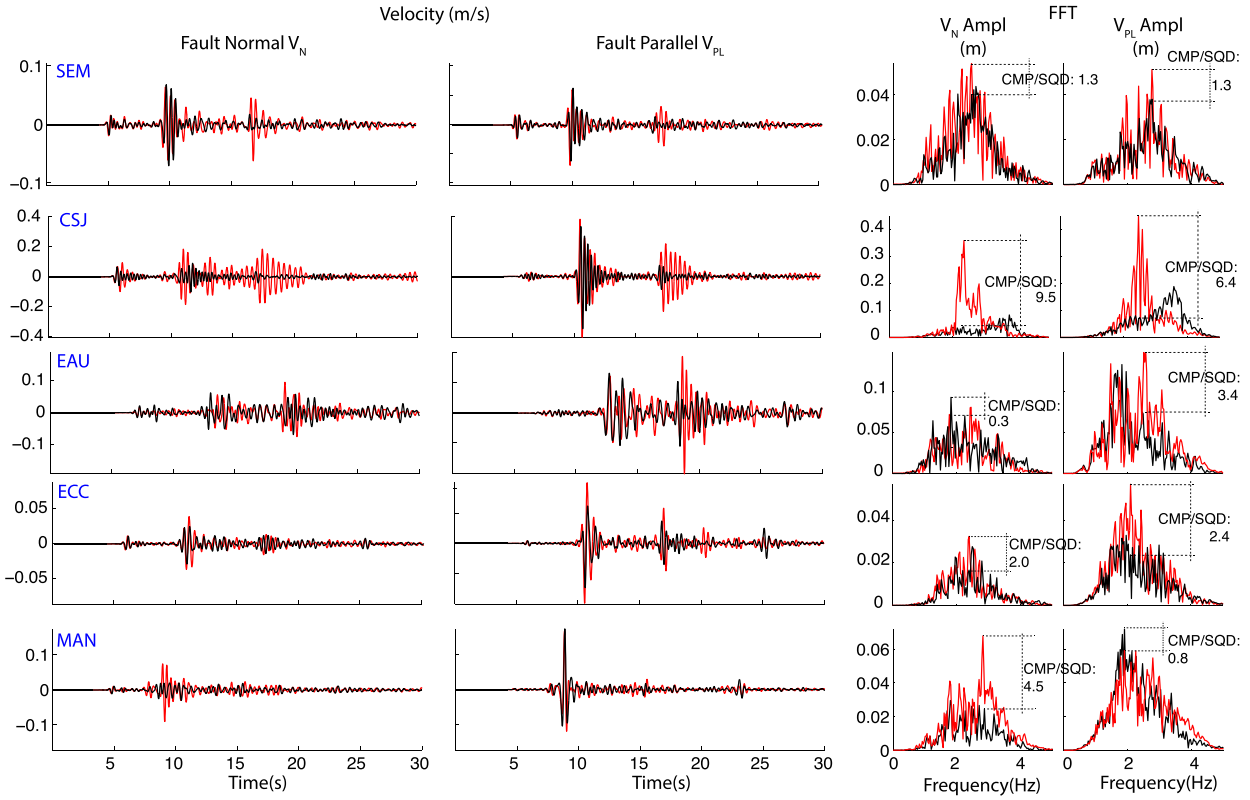

Figure 10. Synthetic time series at five stations of the strong ground motion network of the city of Medellín from earthquake scenario No. 1. Red lines depict results from the CMP simulation. Black lines illustrate SQD results.

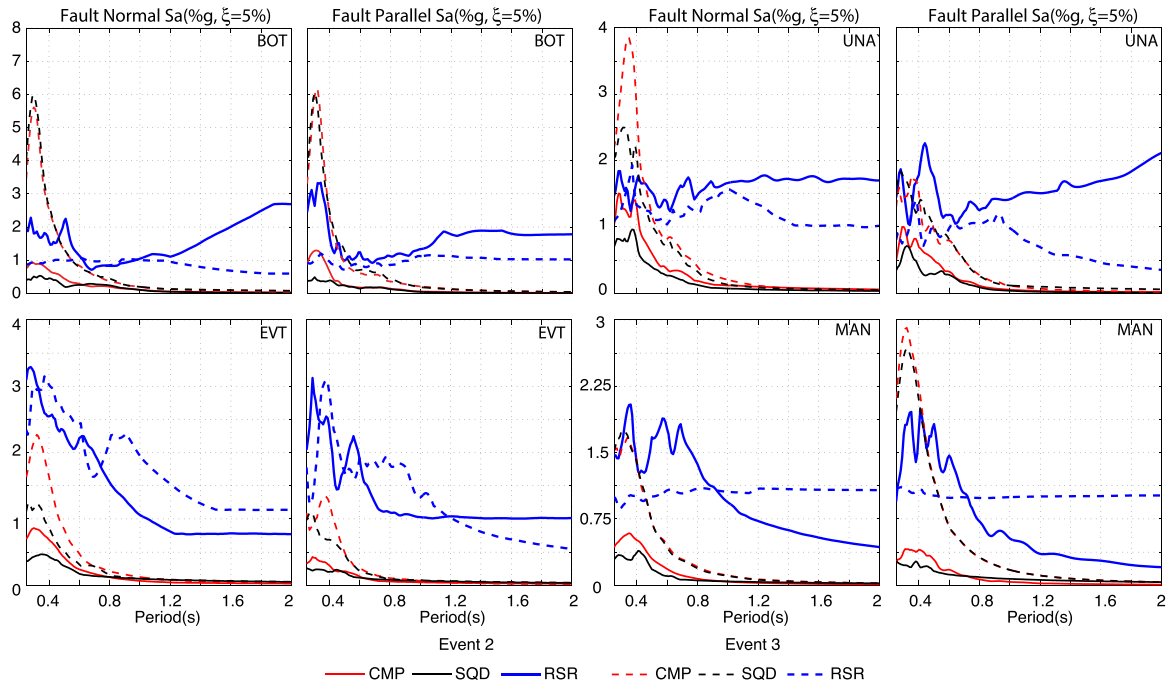

Figure 11. Pseudo-acceleration response spectra S_a(per cent g) (damping $\xi = 5$ per cent) corresponding to ground accelerations from the second event (solid lines), and the third event (dotted lines). Red lines depict results from the CMP simulations, while black lines illustrate results from the SQD findings. Blue lines denote response spectra ratios RSR $= S_{a_{CMP}} / S_{a_{SQD}}$.

EVT and UNA tend to dominate the peak amplitude of the RSR spectra in the short period range where RSR∼3 and RSR∼2 were found. Note that in terms of the RSR, the topographic amplification factor is reasonably constrained in both magnitude and frequency range. Future studies might find useful this redefinition of TAF to examine seismic site response including topographic effects.

CONCLUDING REMARKS

The deterministic 3-D ground motion simulations conducted in the Aburrá Valley, based upon four earthquake rupture scenarios along one segment of the Romeral fault have served to confirm the importance of surface topography on ground motion throughout the region. In particular, our findings for the Aburrá Valley region showed that:

(i) The interaction of surficial topography with near-source scenarios and heterogeneous 3-D velocity structures creates complex patterns of scattering and reflection of seismic energy. As the wavefields propagate through the valley, the interaction with the undulating topography generates a significant number of high-frequency surface waves that continue to reverberate long after the passage of the main wave fronts, and consequently, increase the duration of shaking. This was clearly confirmed in the snapshots of the third earthquake scenario. Here, the characteristics of the rupture directed most of the seismic energy in the NE direction which after crossing the right flank of the Aburrá Valley left a dramatic trail of high amplitude surface waves.

(ii) The impact of topography on the lower parts of the metropolitan area of the Aburá valley is characterized by a tendency towards amplification of the ground motion when compared with results that omit topography. The slopes of the valley act as barriers that bounce back part of the seismic energy into the valley generating zones of constructive/destructive interference. Moreover, it appears that substantial variations of the 3-D velocity structure enhance this behaviour. This was confirmed by the large TAF of up to near 500 per cent that occurred along the free surfaces of sections 30N-30N, and 40N-40N close to strong lateral material interfaces.

(iii) The slopes of the Aburrá Valley exhibit a contrasting distribution of amplifications/reductions, which seem to correlate with source-directivity effects, the steepness of the slope, and local variations of the topographic relief. For instance, along the eastern slopes close to the Envigado municipality our results show spots of amplification, at the same time that the overall behaviour is towards reductions. These reductions are minor and do not exceed 50 per cent. By contrast, the slopes behind the Bello municipality, characterized by steep-slopes and a prominent re-entrant corner, exhibit amplifications that exceed 200 per cent. Similar patterns of amplification are exhibited at other re-entrant corners such as the riverbed of the Santa Elena tributary stream. Of particular note are the reduction areas around the summits of the slopes of the Aburrá valley depression. Global TAF analysis (Fig. 8) and local section analysis performed at the velocity component level (Fig. 9) call into question the general idea of strong amplifications at mountains tops. In both flanks, maxima appear only after the reduction zones have developed. Although an explanation of this phenomenon is not yet clear, our findings suggest that such reductions could be correlated with the local topography, as these deamplifications are mostly accentuated at the eastern plateau towards the SNV, and the northern plateau behind the Bello municipality.

(iv) The San Nicolas Valley region is significantly affected by topographic effects. Located at the eastern side of the domain, this valley exhibits TAFs between 50 and 100 per cent. Some reduction areas were also found, although to a lesser extent. For the San Nicolas Valley, which is located on an elevated plateau, the observed overall amplification pattern is consistent with standard notions of topography effects.

(v) Other factors such as material nonlinearity and intrinsic attenuation could influence our results. During large events, material nonlinearity most likely will reduce the ground motion displacement, followed by the occurrence of plastic zones characterized by the appearance of permanent displacements. The Quaternary deposits of soft soil would be the more affected by this condition. Topography might play a detrimental role in the material response inasmuch as the bounced energy from the foot hills increases the duration of shaking, therefore nonlinear excursions of the soil deposits will also increase. Future analyses are needed in order to properly quantify these interactions.

We understand the idealized nature of our models, and that comparisons with data are desirable. Unfortunately, to date, there are no strong-motion records to validate our results. Our findings, however, underline the impact of topography-related site effects, and their importance in studying the characteristics of ground motion in metropolitan areas located in mountainous regions.

ACKNOWLEDGEMENTS

This work was supported by a National Science Foundation (NSF) grant to SCEC: SI2-SSI: A Sustainable Community Software Framework for Petasacale Earthquake Modeling (ACI-1148493), through a Dean's fellowship from the College of Engineering of Carnegie Mellon University (CMU), a Fulbright fellowship from the Colombian Fulbright-Colciencias-DNP program and additional funding from Universidad EAFIT, the CMU Department of Civil and Environmental Engineering and the Enlaza Mundos program of the city of Medellín. This research was supported by the Southern California Earthquake Center (SCEC). SCEC is funded by NSF Cooperative Agreement EAR-1033462 and USGS Cooperative Agreement G12AC20038. The SCEC contribution number for this paper is 2106. The computations were performed on Kraken at the U.S. National Institute for Computational Sciences (NICS). We also thank an anonymous reviewer for her/his constructive comments and suggestions. These have helped us improve the manuscript and to bring additional clarity to our contribution.

REFERENCES

Aagaard, B. *et al.*, 2008. Ground-motion modeling of the 1906 San Francisco earthquake, Part I: Validation using the 1989 Loma Prieta earthquakes, *Bull. seism. Soc. Am.,* **98**(2), 989–1011.

Acevedo, A., 2011. Construcción de un Modelo Interpretativo 3D hasta 30 km de Profundidad de la Corteza Alrededor del Valle de Aburrá. *Master's thesis,* Universidad EAFIT.

Adams, B.M. & Jaramillo, J.D., 2002. A two-dimensional study on the weak-motion seismic response of the Aburra Valley, Medellín, Colombia, *Bull. N.Z. Soc. Earthq. Eng.,* **35**(1), 17–41.

Aristizábal, E., Roser, B. & Yokota, S., 2005. Tropical chemical weathering of hillslope deposits and bedrock source in the Aburrá Valley, northern Colombian Andes, *Eng. Geol.,* **81**(4), 389–406.

Assimaki, D., Gazetas, G. & Kausel, E., 2005. Effects of local soil conditions on the topographic aggravation of seismic motion: parametric investigation and recorded field evidence from the 1999 Athens earthquakes, *Bull. seism. Soc. Am.,* **95**(3), 1059–1089.

Bao, H., Bielak, J., Ghattas, O., Kallivokas, L.F., O'Hallaron, D.R., Shewchuk, J.R. & Xu, J., 1998. Large-scale simulation of elastic wave propagation in heterogeneous media on parallel computers, *Comput. Methods Appl. Mech. Eng.,* **152,** 85–102.

Barrero, D., Pardo, A., Vargas, C. & Martínez, J., 2007. *Colombian Sedimentary Basins: Nomenclature, Boundaries and Petroleum Geology, a New Proposal,* pp. 78–81, Agencia Nacional de Hidrocarburos.

Betancur, J.J., 2007. Approaches to the regularization of informal settlements: the case of PRIMED in Medellin, Colombia, *Glob. Urban Dev. Mag.,* **3**(1), 1–15.

Bielak, J., Karaoglu, H. & Taborda, R., 2011. Memory-efficient displacement-based internal friction for wave propagation simulation, *Geophysics,* **76**(6), T131–T145.

Borcherdt, R., 1970. Effects of local geology on ground motion near San Francisco Bay, *Bull. seism. Soc. Am.,* **60**(1), 29–61.

Bouchon, M. & Barker, J.S., 1996. Seismic response of a hill: the example of Tarzana, California, *Bull. seism. Soc. Am.,* **86**(1A), 66–72.

Bourgois, J., Calle, B., Tournon, J. & Toussaint, J.-F., 1982. The andean ophiolitic megastructures on the Buga-Buenaventura transverse (Western Cordillera Valle Colombia), *Tectonophysics,* **82**(3), 207–229.

Bourgois, J. *et al.*, 1987. Geological history of the Cretaceous ophiolitic complexes of northwestern South America (Colombian Andes), *Tectonophysics,* **143**(4), 307–327.

Buech, F., Davies, T.R. & Pettinga, J.R., 2010. The Little Red Hill seismic experimental study: topographic effects on ground motion at a bedrock-dominated mountain edifice, *Bull. seism. Soc. Am.,* **100**(5A), 2219–2229.

Çelebi, M., 1987. Topographical and geological amplifications determined from strong-motion and aftershock records of the 3 March 1985 Chile earthquakes, *Bull. seism. Soc. Am.,* **77**(4), 1147–1167.

Çelebi, M. *et al.*, 2010. Recorded motions of the 6 April 2009 M_w 6.3 L'Aquila, Italy, earthquake and implications for building structural damage: overview, *Earthq. Spectra,* **26**(3), 651–684.

Davis, L. & West, L., 1973. Observed effects of topography on ground motion, *Bull. seism. Soc. Am.,* **63**(1), 283–298.

Donati, S., Marra, F. & Rovelli, A., 2001. Damage and ground shaking in the town of Nocera Umbra during Umbria-Marche, central Italy, earthquakes: the special effect of a fault zone, *Bull. seism. Soc. Am.,* **91**(3), 511–519.

Echeverry, A. & Orsini, F., 2010, Informalidad y Urbanismo Social en Medellin, in *Medio Ambiente, Urbanismo y Sociedad*, pp. 130–152, eds Hermelin, M., Echeverry, A. & Giraldo, J., Universidad EAFIT, Medellin.

Farbiarz, J., Jaramillo, J.D. & Villarraga, M.R., 2000. Microzonation of the city of Medellín, in *Proc. 12th World Conference on Earthquake Engineering*, New Zealand.

Field, E. & Jacob, K., 1995. A comparison and test of various site-response estimation techniques, including three that are not reference-site dependent, *Bull. seism. Soc. Am.,* **85**(4), 1127–1143.

Freymueller, J.T., Kellogg, J.N. & Vega, V., 1993. Plate motions in the North Andean region, *J. geophys. Res.,* **98**(B12), 21 853–21 863.

Gao, S., Liu, H., Davis, P. & Knopoff, L., 1996. Localized amplification of seismic waves and correlation with damage due to the Northridge earthquake: Evidence for focusing in Santa Monica, *Bull. seism. Soc. Am.,* **86**(1B), S209–S230.

Geli, L., Bard, P.-Y. & Jullien, B., 1988. The effect of topography on earthquake ground motion: A review and new results, *Bull. seism. Soc. Am.,* **78**(1), 42–63.

GSM, 1999. Grupo de Sismología de Medellín. Instrumentación y Microzonificación Sísmica del área Urbana de Medellín. Technical report, Sistema Municipal para la Prevención y Atención de Desastres, Alcaldía de Medellín.

GSM, 2006. Grupo de Sismología de Medellín: Microzonificación Sísmica Detallada de los Municipios de Barbosa, Girardota, Copacabana, Sabaneta, La Estrella, Caldas y Envigado. Technical report, Área Metropolitana del Valle de Aburrá.

Gvirtzman, Z. & Louie, J.N., 2010. 2D Analysis of Earthquake Ground Motion in Haifa Bay, Israel, *Bull. seism. Soc. Am.,* **100**(2), 733–750.

Hartzell, S., Cranswick, E., Frankel, A., Carver, D. & Meremonte, M., 1997. Variability of site response in the Los Angeles urban area, *Bull. seism. Soc. Am.,* **87**(6), 1377–1400.

Hartzell, S.H., Carver, D.L. & King, K.W., 1994. Initial investigation of site and topographic effects at Robinwood Ridge, California, *Bull. seism. Soc. Am.,* **84**(5), 1336–1349.

Hough, S.E., Yong, A., Altidor, J.R., Anglade, D., Given, D. & Mildor, S.-L., 2011. Site characterization and site response in Port-au-Prince, Haiti, *Earthq. Spectra,* **27**(S1), S137–S155.

Kawase, H. & Aki, K., 1990. Topography effect at the critical SV-wave incidence: Possible explanation of damage pattern by the Whittier Narrows, California, earthquake of 1 October 1987, *Bull. seism. Soc. Am.,* **80**(1), 1–22.

Kellogg, J.N. & Vega, V., 1995. Tectonic development of Panama, Costa Rica, and the Colombian andes: Constraints from global positioning system geodetic studies and gravity, *Geological Society of America Special Paper,* **295,** 75–90.

Komatitsch, D., Liu, Q., Tromp, J., Süss, P., Stidham, C. & Shaw, J.H., 2004. Simulations of ground motion in the Los Angeles basin based upon the spectral-element method, *Bull. seism. Soc. Am.,* **94**(1), 187–206.

Lee, S., Komatitsch, D., Huang, B. & Tromp, J., 2009a. Effects of topography on seismic-wave propagation: An example from northern Taiwan, *Bull. seism. Soc. Am.,* **99**(1), 314–325.

Lee, S.-J., Chen, H.-W., Liu, Q., Komatitsch, D., Huang, B.-S. & Tromp, J., 2008. Three-dimensional simulations of seismic-wave propagation in the Taipei basin with realistic topography based upon the spectral-element method, *Bull. seism. Soc. Am.,* **98**(1), 253–264.

Lee, S.-J., Chan, Y.-C., Komatitsch, D., Huang, B.-S. & Tromp, J., 2009b. Effects of realistic surface topography on seismic ground motion in the Yangminshan region of Taiwan based upon the spectral-element method and LiDAR DTM, *Bull. seism. Soc. Am.,* **99**(2A), 681–693.

Lovati, S., Bakavoli, M., Massa, M., Ferretti, G., Pacor, F., Paolucci, R., Haghshenas, E. & Kamalian, M., 2011. Estimation of topographical effects at Narni ridge (Central Italy): comparisons between experimental results and numerical modelling, *Bull. Earthq. Eng.,* **9**(6), 1987–2005.

Ma, S., Archuleta, R.J. & Page, M.T., 2007. Effects of large-scale surface topography on ground motions, as demonstrated by a study of the San Gabriel mountains, Los Angeles, California, *Bull. seism. Soc. Am.,* **97**(6), 2066–2079.

Maufroy, E., Cruz-Atienza, V. & Gaffet, S., 2012. A robust method for assessing 3-D topographic site effects: a case study at the LSBB underground laboratory, France, *Earthq. Spectra,* **28**(3), 1097–1115.

Maya, M. & Gonzales, H., 1995. Unidades litodémicas en la Cordillera Central de Colombia, *Boletín Geológico,* **35,** 43–57.

McCourt, W., Aspden, J. & Brook, M., 1984. New geological and geochronological data from the Colombian Andes: continental growth by multiple accretion, *J. Geol. Soc.,* **141**(5), 831–845.

NSR-10 2010, *Reglamento Colombiano de Construcción Sismo Resistente. NSR-10*. Ley 400 de 1997.

Osorio, F.A., 2015. Modelo de Exposición de Viviendas del Departamento de Antioquia, Colombia, *Master's thesis,* Universidad EAFIT.

Paolucci, R., 2002. Amplification of earthquake ground motion by steep topographic irregularities, *Earthq. Eng. Struct. Dyn.,* **31**(10), 1831–1853.

París, G., Machette, R., Dart, R. & Haller, K., 2000. Database and map of Quaternary faults and folds of Colombia and its offshore regions, Open–file Report 00–0284.

Pedersen, H., Le Brun, B., Hatzfeld, D., Campillo, M. & Bard, P., 1994. Ground-motion amplitude across ridges, *Bull. seism. Soc. Am.,* **84**(6), 1786–1800.

Pischiutta, M., Cultrera, G., Caserta, A., Luzi, L. & Rovelli, A., 2010. Topographic effects on the hill of Nocera Umbra, central Italy, *Geophys. J. Int.,* **182**(2), 977–987.

Pulido, N., 2003. Seismotectonics of the northern Andes (Colombia) and the development of seismic networks, *Bulletin of the International Institute of Seismology and Earthquake Engineering,* special edition, 69–76.

Quinay, P., Ichimura, T. & Hori, M., 2012. Waveform inversion for modeling three-dimensional crust structure with topographic effects, *Bull. seism. Soc. Am.,* **102**(3), 1018–1029.

Ramírez, J.E., 1975. Historia de los terremotos en Colombia, *Documentación Geográfica*.

Restrepo, D. & Bielak, J., 2014. Virtual topography: a fictitious domain approach for analyzing free-surface irregularities in large-scale earthquake ground motion simulation, *Int. J. Numer. Methods Eng.,* **100**(7), 504–533.

Rozycki, P., Moës, N., Bechet, E. & Dubois, C., 2008. X-FEM explicit dynamics for constant strain elements to alleviate mesh constraints on internal or external boundaries, *Comput. Methods Appl. Mech. Eng.,* **197**(5), 349–363.

Saulev, V.K., 1963. On solution of some boundary value problems on high performance computers by fictitious domain method, *Siberian Math. J.,* **4**(4), 912–925 (in Russian).

Serrano, R., 2014. DAMIAN-PAR: A numerical tool for the simulation of wave propagation problems over large scale seismic scenarios based upon the finite element method, *Master's thesis,* Universidad EAFIT.

Shani-Kadmiel, S., Tsesarsky, M., Louie, J.N. & Gvirtzman, Z., 2012. Simulation of seismic-wave propagation through geometrically complex basins: the Dead Sea Basin, *Bull. seism. Soc. Am.,* **102**(4), 1729–1739.

Shunn, L. & Ham, F., 2012. Symmetric quadrature rules for tetrahedra based on a cubic close-packed lattice arrangement, *J. Comput. Appl. Math.,* **236**(17), 4348–4364.

Spudich, P., Hellweg, M. & Lee, W. H.K., 1996. Directional topographic site response at Tarzana observed in aftershocks of the 1994 Northridge, California, earthquake: implications for mainshock motions, *Bull. seism. Soc. Am.,* **86**(1B), S193–S208.

Taboada, A., Rivera, L.A., Fuenzalida, A., Cisternas, A., Philip, H., Bijwaard, H., Olaya, J. & Rivera, C., 2000. Geodynamics of the Northern Andes: subductions and intracontinental deformation (Colombia), *Tectonics,* **19**(5), 787–813.

Tu, T., Yu, H., Ramirez-Guzman, L., Bielak, J., Ghattas, O., Ma, K.-L. & O'Hallaron, D.R., 2006. From mesh generation to scientific visualization: an end-to-end approach to parallel supercomputing, in *Proceedings of the 2006 ACM/IEEE conference on Supercomputing,* p. 91, ACM.

Tucker, B., King, J., Hatzfeld, D. & Nersesov, I., 1984. Observations of hard-rock site effects, *Bull. seism. Soc. Am.,* **74**(1), 121–136.